Communication

Development of the Recursive Convolutional CFS-PML for the Wave-Equation-Based Meshless Method

Jun-Feng Wang, Zhizhang David Chen, Cheng Peng, Jinyan Li, and Sergey A. Ponomarenko

Abstract—In this communication, the recursive convolutional complex frequency shifted perfectly matched layer (CFS-PML) absorbing boundary condition (ABC) is developed for the wave-equation-based meshless method. The numerical results show that the proposed CFS-PML can achieve an excellent absorption performance with the reflections less than -52.5 dB when the six layers of the PML are applied, and less than -57.3 dB when ten layers of the PML are applied (including operations with evanescent waves). The impacts of the CFS-PML parameters, shape parameter, and different node distribution types are also investigated. Such performances allow the use of the wave-equation-based meshless method for solving open problems.

Index Terms—Absorbing boundary condition (ABC), complex frequency shifted (CFS), perfectly matched layer (PML), the node-based meshless method, wave equation.

I. INTRODUCTION

Without any doubt, accurate electromagnetic numerical methods have made designs of modern electronic circuits and microwave devices more efficient and effective. The conventional grid- or mesh-based numerical methods have been developed and widely used for microwave and electromagnetic structures modelings, such as the finite-difference time-domain (FDTD) method [1], the finite element method (FEM) method [2], and the method of moment (MoM) [3]. However, when dealing with conformal boundary problems, the conventional mesh-based methods need predefined meshes to provide particular relationships between spatial nodes, and meshing processes can be challenging and problematic in practice. Moreover, once a mesh is defined, it is hard to conduct partial or local mesh refinements to capture property variations of a subregion.

To overcome the above two shortcomings, the node-based meshless methods were proposed in recent years [4]–[7]. Due to its relative simplicity and easy treatment of boundary conditions, the radial point interpolation meshless (RPIM) method has attracted more attention [8]–[10] than other meshless methods. Toward this end, Yang *et al.* [11] report the divergence-free meshless method to remove the possible spurious numerical solutions. Shams *et al.* [12] describe a dispersive time-domain meshless formulation for simulating linear frequency-dependent materials. Moreover, Yu and Chen [13] develop the perfectly matched layer (PML) absorbing boundary condition (ABC) for the unconditionally stable meshless method.

In the above meshless methods, the first-order Maxwell's equations are directly solved; as a result, electric and magnetic field nodes are positioned spatially in a staggering manner. Such a spatial node arrangement can be time-consuming for large and complex structures. It may also pose a problem at a boundary where conditions are defined jointly and colocated for all the electric and magnetic fields. To address the staggered-field issue, Yang *et al.* [14] and Khalef *et al.* [15] propose a node collocated time-domain RPIM method, which is based on the wave equation. In it, instead of solving Maxwell's equations directly that involve all the coupled field components, the decoupled wave equation for electric fields or magnetic fields only is numerically solved. Consequently, only the nonstaggered electric field nodes need to be defined and computed. Along the same line, Lombardi *et al.* [16], [17] develop the wave-equation-based meshless method for modeling homogeneous and inhomogeneous waveguides based on the variational principle.

In spite of the above developments, there still lack the ABCs, especially the complex-frequency-shifted (CFS)-PMLs [18]–[21], for the wave-equation-based time-domain meshless methods. In this communication, we develop the recursive convolutional CFS-PML ABC for the wave-equation-based meshless method and numerically verify its effectiveness.

The PML schemes have been developed for the meshless methods that solve the first-order Maxwell's equations directly [22]–[24]. They cannot be applied directly to the wave-equation-based meshless methods. This communication fills in the void and successfully develops the CFS-PML ABC for the wave-equation-based meshless methods. It not only verifies the effectiveness of the proposed CFS-PML ABC but also presents the parametric study of its absorption performance. As a result, the wave-equation-based meshless method can now be applied to open problems.

It is worth to mention that the wave-equation-based meshless method with the CFS-PML [25], [26] has the following advantages over the conventional FDTD method with the CFS-PMLs:

1) the FDTD method essentially uses low-order basis function (rooftop function) to expand the field quantities, while the meshless method uses high-order basis function (Gaussian function); the meshless method has smaller numerical errors than the FDTD method [8], [10], [14];

2) the FDTD grid is not conformal with irregular boundaries and not easy for local or regional mesh refinements, while the meshless method is node-based and has relative good flexibility in handling different boundary shapes and conditions and in imposing node refinements;

3) the meshless method allows the selections of different basis functions for spatial discretization, making it more adaptable to different types of problems [8] and easier hybridization of different methods [30].

This communication is organized in the following manner. In Section II, the proposed recursive convolutional CFS-PML ABC is derived with the introduction of auxiliary variables. In Section III, the effectiveness of the proposed CFS-PML is verified, and a parametric study is conducted with different CFS-PML parameters, shape parameters of the meshless method, and different node distributions. Finally, conclusion and discussion are made in Section IV.

II. FORMULATIONS OF THE PROPOSED RECURSIVE CONVOLUTIONAL CFS-PML ABC

For simplicity, we formulate the proposed recursive convolutional CFS-PML ABC in 2-D and take the 2-D transverse-magnetic case for easy demonstrations. Consider the 2-D wave equation for electric field E_z in a homogeneous, lossless, and source-free medium

$$\nabla^2 E_z - \mu\varepsilon \frac{\partial^2 E_z}{\partial t^2} = 0 \tag{1}$$

where μ and ε represent medium's permeability and permittivity, respectively.

In the PML regions, we introduce the second-order stretched-coordinate complex operator, which is expressed as

$$\nabla_s^2 = \frac{1}{s_x}\frac{\partial}{\partial x}\left(\frac{1}{s_x}\frac{\partial}{\partial x}\right) + \frac{1}{s_y}\frac{\partial}{\partial y}\left(\frac{1}{s_y}\frac{\partial}{\partial y}\right) \tag{2}$$

with the stretched-coordinate factor [18]

$$s_w = \kappa_w + \frac{\sigma_w}{a_w + j\omega\varepsilon_0} \tag{3}$$

where w is x or y, κ_w is the stretched coordinate coefficient which is real and larger than 1, σ_w is electric conductivity, and a_w is the shifting parameter.

The CFS-PML wave equation is obtained by substituting (2) into (1). However, direct computation of the resulting equation is not easy. Here, we introduce the following auxiliary variables A_{x1}, A_{x2}, A_{y1}, and A_{y2} to perform the PML computation

$$j\omega A_{x1} = \frac{1}{s_x}\frac{\partial E_z}{\partial x} \tag{4}$$

$$j\omega A_{x2} = \frac{1}{s_x}\frac{\partial}{\partial x}(j\omega A_{x1}) \tag{5}$$

$$j\omega A_{y1} = \frac{1}{s_y}\frac{\partial E_z}{\partial y} \tag{6}$$

$$j\omega A_{y2} = \frac{1}{s_y}\frac{\partial}{\partial y}(j\omega A_{y1}). \tag{7}$$

We now substitute (4)–(7) into (1), apply the inverse Fourier transform, and obtain the proposed CFS-PML equation

$$\frac{\partial^2 E_z}{\partial t^2} = \frac{1}{\mu\varepsilon}\frac{\partial}{\partial t}(A_{x2} + A_{y2}). \tag{8}$$

In the following paragraphs, we derive the equations for computing A_{x2} and A_{y2}.

First, we apply the inverse Fourier transform to (4) and obtain

$$\frac{\partial A_{x1}}{\partial t} = s_x^*(t) * \frac{\partial E_z}{\partial x} \tag{9}$$

where

$$s_x^*(t) = \frac{\delta(t)}{\kappa_x} + \zeta_x(t)$$

$$\zeta_x(t) = -\frac{\sigma_x}{\varepsilon_0\kappa_x^2}e^{-a_x t}u(t)$$

$$a_x = \frac{\sigma_x}{\varepsilon_0\kappa_x} + \frac{a_x}{\varepsilon_0}$$

Here, $\delta(t)$ represents the Dirac impulse function, and $u(t)$ represents the unit step function.

We can expand (9) by applying the property of the Dirac impulse function

$$\frac{\partial A_{x1}(t, x, y)}{\partial t} = \frac{1}{\kappa_x}\frac{\partial E_z(t, x, y)}{\partial x} + \psi_{x1}(t, x, y) \tag{10}$$

where

$$\psi_{x1}(t, x, y) = \zeta(t, x, y) * \frac{\partial E_z(t, x, y)}{\partial t} \tag{11}$$

(11) can be computed numerically in a recursive manner

$$\begin{aligned}
\psi_{x1}(t, x, y)|_{t=n\Delta} &= \zeta(t) * \frac{\partial E_z(t, x, y)}{\partial t}\Big|_{t=n\Delta t} \\
&= c_x \frac{\partial E_z(t, x, y)}{\partial x}\Big|_{t=n\Delta t} \\
&\quad + e^{-a_x\Delta t}\psi_{x1}(t, x, y)|_{t=(n-1)\Delta t}
\end{aligned} \tag{12}$$

with

$$c_x = \frac{\sigma_x}{\kappa_x(\sigma_x + \kappa_x a_x)}\left(e^{-a_x\Delta t} - 1\right).$$

In solving the above equations, electric field nodes are predefined. For convenience, we define them like that for the point-matched time-domain FEM presented in [27]. Then, the electric field E_z is approximated as

$$E_z(\mathbf{r}) = \sum_{m=1}^{M} r_m(\mathbf{r}) a_m = \mathbf{R}(\mathbf{r})\,\mathbf{a} \tag{13}$$

where $\mathbf{r} = (x, y)$ is the point of interest at which E_z is to be interpolated, $r_m(\mathbf{r})$ is the radial basis function associated with node m (we choose Gaussian function), a_m is the expansion coefficients to be found, and M is the number of electric fields nodes within the support domain.

With the meshless formulation [10], [14], (13) can be rewritten as

$$\begin{aligned}
E_z(\mathbf{r}) &= \sum_{m=1}^{M} \phi_m(x, y) E_{z,m}^n \\
&= \mathbf{\Phi}(\mathbf{r})\,\mathbf{E}_{sz}(\mathbf{r})
\end{aligned} \tag{14}$$

where $\mathbf{E}_{sz}(\mathbf{r})$ is the unknown electric field value vector to be found, and the shape function vector $\mathbf{\Phi}(\mathbf{r})=[\varphi_1(\mathbf{r}), \varphi_2(\mathbf{r}),\ldots, \varphi_M(\mathbf{r})] = \mathbf{R}\mathbf{G}^{-1}$ with

$$\mathbf{G} = \begin{bmatrix}
r_1(x_1, y_1) & r_2(x_1, y_1) & \cdots & r_M(x_1, y_1) \\
r_1(x_2, y_2) & r_2(x_2, y_2) & \cdots & r_M(x_2, y_2) \\
\vdots & \vdots & & \vdots \\
r_1(x_M, y_M) & r_2(x_M, y_M) & \cdots & r_M(x_M, y_M)
\end{bmatrix}. \tag{15}$$

Once the shape function $\mathbf{\Phi}(\mathbf{r})$ is found (it is time-invariant), the first-order partial derivative can be analytically found as

$$\frac{\partial\mathbf{\Phi}}{\partial x} = \frac{\partial\mathbf{R}}{\partial x}\mathbf{G}^{-1}. \tag{16}$$

The above meshless method using Gaussian basis function has been proven to be efficient and more accurate than the FDTD method for electromagnetic modeling [10], [14].

By substituting (16) into (10) and (12), respectively, and using the central finite-difference to replace the time derivative, we can get the final discretization formulations for ψ_{x1} and A_{x1}

$$\psi_{x1,i}^{n+\frac{1}{2}} = c_x \sum_{m=1}^{M} E_{z,m}^n \frac{\partial \phi_m}{\partial x} + e^{-\alpha_x \Delta t} \psi_{x1,i}^{n-\frac{1}{2}} \tag{17}$$

$$A_{x1,i}^{n+\frac{1}{2}} = A_{x1,i}^{n-\frac{1}{2}} + \frac{\Delta t}{\kappa_x} \sum_{m=1}^{M} E_{z,m}^n \frac{\partial \phi_m}{\partial x} + \Delta t \psi_{x1,i}^{n+\frac{1}{2}} \tag{18}$$

where φ_m represents the shape function associated with node m in the local finite support domain.

The formulations for computing auxiliary variables A_{x2}, A_{y1}, and A_{y2} can be derived in a similar way, and results are as follows

$$\psi_{x2,i}^{n+\frac{1}{2}} = \frac{c_x}{\Delta t} \sum_{m=1}^{M} \left(A_{x1,m}^{n+\frac{1}{2}} - A_{x1,m}^{n-\frac{1}{2}} \right) \frac{\partial \phi_m}{\partial x} + e^{-\alpha_x \Delta t} \psi_{x2,i}^{n-\frac{1}{2}} \tag{19}$$

$$A_{x2,i}^{n+\frac{1}{2}} = A_{x2,i}^{n-\frac{1}{2}} + \frac{1}{\kappa_x} \sum_{m=1}^{M} \left(A_{x1,m}^{n+\frac{1}{2}} - A_{x1,m}^{n-\frac{1}{2}} \right) \frac{\partial \phi_m}{\partial x} + \Delta t \psi_{x2,i}^{n+\frac{1}{2}} \tag{20}$$

$$\psi_{y1,i}^{n+\frac{1}{2}} = c_y \sum_{m=1}^{M} E_{z,m}^n \frac{\partial \phi_m}{\partial y} + e^{-\alpha_y \Delta t} \psi_{y1,i}^{n-\frac{1}{2}} \tag{21}$$

$$A_{y1,i}^{n+\frac{1}{2}} = A_{y1,i}^{n-\frac{1}{2}} + \frac{\Delta t}{\kappa_y} \sum_{m=1}^{M} E_{z,m}^n \frac{\partial \phi_m}{\partial y} + \Delta t \psi_{y1,i}^{n+\frac{1}{2}} \tag{22}$$

$$\psi_{y2,i}^{n+\frac{1}{2}} = \frac{c_y}{\Delta t} \sum_{m=1}^{M} \left(A_{y1,m}^{n+\frac{1}{2}} - A_{y1,m}^{n-\frac{1}{2}} \right) \frac{\partial \phi_m}{\partial y} + e^{-\alpha_y \Delta t} \psi_{y2,i}^{n-\frac{1}{2}} \tag{23}$$

$$A_{y2,i}^{n+\frac{1}{2}} = A_{y2,i}^{n-\frac{1}{2}} + \frac{1}{\kappa_y} \sum_{m=1}^{M} \left(A_{y1,m}^{n+\frac{1}{2}} - A_{y1,m}^{n-\frac{1}{2}} \right) \frac{\partial \phi_m}{\partial y} + \Delta t \psi_{y2,i}^{n+\frac{1}{2}}. \tag{24}$$

With them applied to (8), we obtain the PML equation for the wave-equation-based meshless method

$$E_{z,i}^{n+1} = 2E_{z,i}^n - E_{z,i}^{n-1} + \frac{\Delta t}{\mu \varepsilon} \left(A_{x2,i}^{n+\frac{1}{2}} + A_{y2,i}^{n+\frac{1}{2}} \right). \tag{25}$$

Note that the ψ_{x1} nodes and the A_{x1} nodes are positioned in between the two neighboring E_z nodes in the x-direction; the ψ_{y1} and A_{y1} nodes are positioned in between the two neighboring E_z nodes in the y-direction; the ψ_{x2}, ψ_{y2}, A_{x2}, and A_{y2} nodes are located at the same position of the E_z nodes.

In summary, the computational flowchart of the proposed recursive convolutional CFS-PML computation is as follows:

1) Update the auxiliary variables ψ_{x1} and ψ_{y1} using (17) and (21).
2) Update the auxiliary variables A_{x1} and A_{y1} using (18) and (22).
3) Update the auxiliary variables ψ_{x2} and ψ_{y2} using (19) and (23).
4) Update the auxiliary variables A_{x2} and A_{y2} using (20) and (24).
5) Update the electric field E_z using (25).
6) Repeat the above operations for each PML layer.

III. NUMERICAL RESULTS

To validate the performance of the proposed CFS-PML scheme for the wave-equation-based meshless method, a TMz-polarized current source propagation numerical experiment is conducted first. The experimental setup is shown in Fig. 1. The solution domain of air is discretized with 101×101 regular nodes, and the nodal spacing is 1.5 mm. A CFS-PML absorbing medium with the same nodal spacing encloses the solution domain to absorb electromagnetic
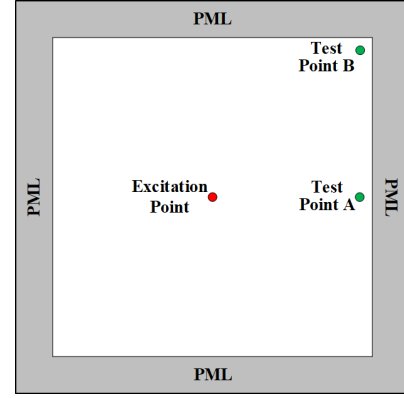

Fig. 1. 2-D free-space excited with a TMz-polarized electric current source.

waves. The shape parameter of the Gaussian basis function (it controls the decaying rate of Gaussian function [14]) and the radius of the local support domain are chosen to be 4.5 and 1.5 mm, respectively. The simulated electric fields are recorded at two test points within the solution domain (see Fig. 1). Test point A is located at the position one node away from the right PML; test point B is located in the top right corner of the solution domain. A Gaussian-modulated sinusoidal pulse excited at the center of the solution domain, which can be expressed as $J_z = \cos(2\pi f_m t)\exp(-(t - t_d)^2 \tau^{-2})$ with $f_m = 10$ GHz, $\tau = 4/\pi/f_m$, and $t_d = 4\tau$.

The electromagnetic wave absorption performance of the proposed CFS-PML scheme depends on the stretched-coordinate factor s_w of (2), which depends on parameters σ, k, and a. Within the CFS-PML medium, the PML parameters are selected and scaled as follows:

$$\sigma_{w,i}(r_{w,i}) = \sigma_w^{max} \left(\frac{r_{w,i}}{d} \right)^n \tag{26}$$

$$\kappa_{w,i}(r_{w,i}) = 1 + \left(\kappa_w^{max} - 1 \right) \left(\frac{r_{w,i}}{d} \right)^n \tag{27}$$

$$a_{w,i}(r_{w,i}) = a_w^{max} \left(\frac{r_{w,i}}{d} \right) \tag{28}$$

where i represents the ith layer of the PML, $w = x$ or y, $r_{w,i}$ is the distance between the ith PML node and the interface between the PML medium and the solution domain, d is the total thickness of the CFS-PML region, and n is the order of scaling profile. The choice of σ_{opt} [1], [21] is taken to be $(n + 1)(150\pi\Delta s)$ where Δs is the nodal spacing.

First, the electric fields are computed with six and eight layers of the CFS-PML medium. The reference solution is also included for comparison; it is obtained in a very large computational domain bounded by the PEC walls with the same source configuration; the domain is so large that the waves reflected from the PEC boundaries do not reach the test point before the simulation is terminated. The CFS-PML parameters are $n = 4$, $\sigma_{max} = 2 \sigma_{opt}$, $\kappa_{max} = 5$, and $a_{max} = 0.05$, respectively.

The time-dependent electric field E_z at point B is plotted in Fig. 2. It is easy to see, in general, the electric fields obtained with six and eight layers of the PML match very well with the reference solution. However, when we zoomed-in view the signal tails, the difference between the results with the proposed CFS-PML and the reference solution can be observed. As shown in Fig. 2, the results calculated with the proposed scheme match better with the reference solution than the results obtained by the FDTD method with the PML medium [19]. Furthermore, the solution obtained with eight layers of the CFS-PML medium matches better with the reference solution than the result with six layers of the CFS-PML
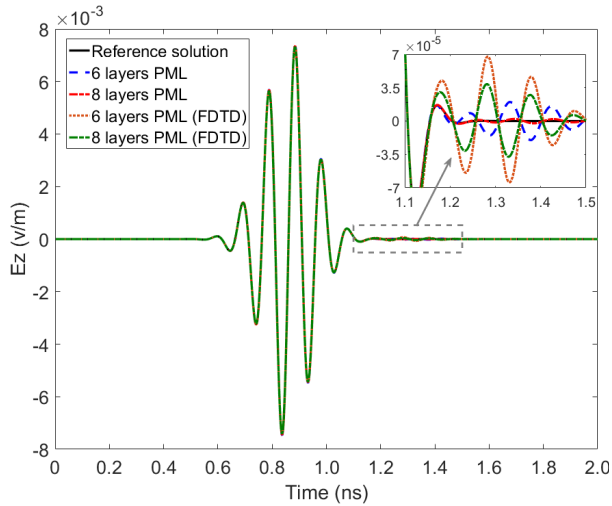
Fig. 2. Time-dependent E_z fields recorded at observation point B with six and eight layers of the CFS-PML ($n = 4$, $\sigma_{max}/\sigma_{opt} = 2$, $k_{max} = 5$, and $a_{max} = 0.05$). The reference solution is also included for comparison.

ABC. It demonstrates that better absorption performance can be obtained by more CFS-PML layers.

As can be seen from Fig. 3(a), the relative reflection error [22] at point A is less than -81 dB when we apply four layers of the PML, and it is less than -165.4 dB when we apply eight layers of the PML; the reflection error is -78.4 and -104 dB when we employ the FDTD method with four and eight layers PML [19]. As shown in Fig. 3(b), at test point B, the reflection error is less than -76.6 and -151.5 dB when we apply four and eight layers of the PML; the reflection error is -68.6 and -97 dB when the FDTD method with four and eight layers PML is conducted. The relative reflection errors measured at test point A are less than those measured at test point B. This is because normally incident waves dominate at test point A for which the CFS-PML ABC has better absorption capacity. Overall, the CFS-PML for the wave-equation-based meshless method has excellent absorption performance and better capacity than the PML medium for the FDTD method.

Next, the effects of the CFS-PML parameters n, k_{max}, and σ_{max} on the absorption performance are investigated. We choose the measurement results at test point B with eight layers of the CFS-PML ABC Fig. 4 presents contours of the maximum relative reflection error in decibel as a function of n and $\sigma_{max}/\sigma_{opt}$, with $k_{max} = 5$ and $a_{max} = 0.05$. Fig. 5 plots contours of the maximum reflection error as a function of k_{max} and $\sigma_{max}/\sigma_{opt}$, when $n = 4$ and $a_{max} = 0.05$. It can be observed that a maximum relative reflection error of -150 dB or less is achieved by selecting $n = 4$ and $\sigma_{max}/\sigma_{opt} = 1$. As seen, $k_{max} = 3$ and $\sigma_{max}/\sigma_{opt} = 1$ give the maximum relative reflection error of less than -160 dB. Based on above parameters analyze results (see Figs. 4 and 5), the proposed recursive convolutional CFS-PML ABC can obtain better absorption in the case studied when PML parameters $\sigma_{max}/\sigma_{opt} = 0.5 \sim 3$, $n = 3 \sim 5$, and $k_{max} = 1 \sim 10$, respectively.

The shape parameter of the wave-equation meshless method controls the decaying rate of the Gaussian basis function [14]. To further study the performance of the proposed node-based CFS-PML ABC scheme, we also investigate how the shape parameter affects electromagnetic wave absorption. As seen in Fig. 6, when the shape parameter varies from 2 to 20, the maximum reflection error at test point A increases monotonously from -166.9 to -140.3 dB. However, at test point B, the maximum reflection error decreases from -148.6 to -151.7 dB when the shape parameter varies from 1.5 to 5; then, it increases to -132.2 dB when the shape parameter
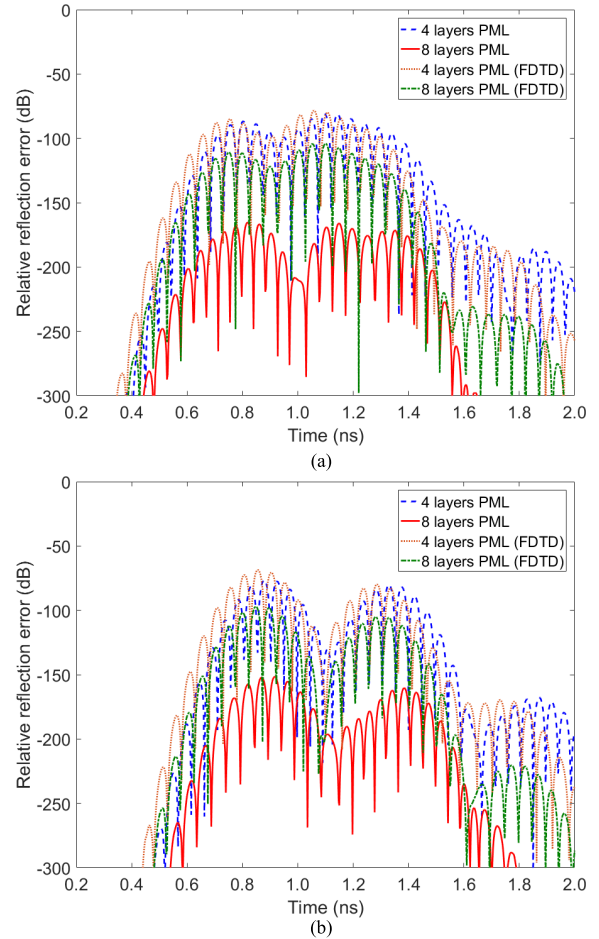

Fig. 3. Relative reflection errors versus time obtained with the proposed CFS-PML scheme with different PML layers ($n = 4$, $\sigma_{max}/\sigma_{opt} = 2$, $k_{max} = 5$, and $a_{max} = 0.05$). (a) At test point A. (b) At test point B.
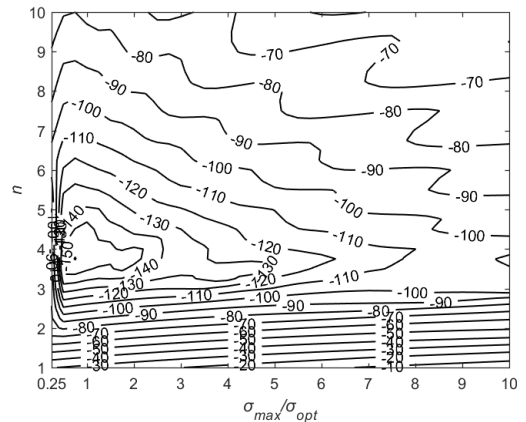

Fig. 4. Contour plot of the maximum relative reflection error of eight layers of the PML in decibel as a function of n and σ_{max} (with $k_{max} = 5$ and $a_{max} = 0.05$).

varies from 5 to 20. It is evident that the proposed CFS-PML gets better electromagnetic wave absorption when the shape parameter is chosen to be in the range of $3 \sim 7$. Nevertheless, in all the cases, the reflection errors are very small, less than -100 dB, enabling the effective use of the proposed CFS-PML without much dependence on the shape parameters.

Next, a numerical experiment is conducted to see how the meshless node distributions affect PML absorption. This is done conveniently with the meshless method since the nonuniform node distributions
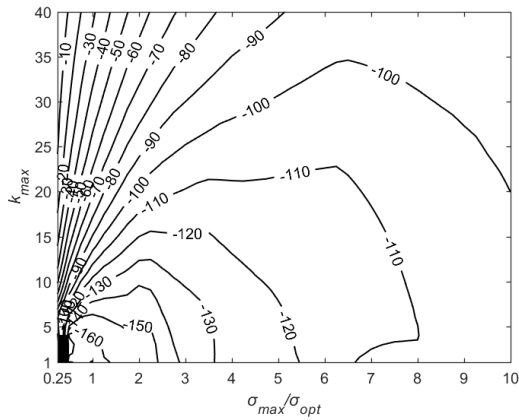
Fig. 5. Contour plot of the maximum relative reflection error of eight layers of the PML in decibel as a function of κ_{max} and σ_{max} (with $n = 4$ and $a_{max} = 0.05$).
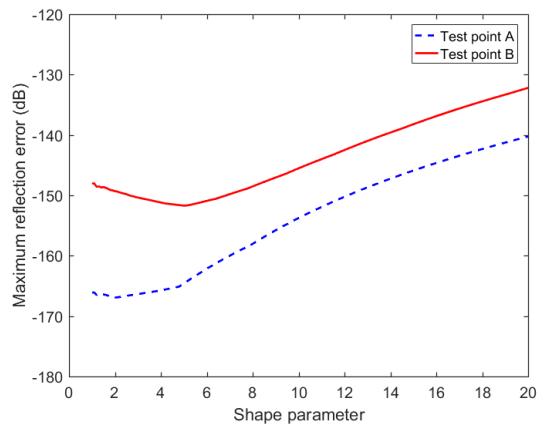

Fig. 6. Maximum reflection errors versus shape parameter obtained with the proposed CFS-PML ($n = 4$, $\sigma_{max}/\sigma_{opt} = 2$, $\kappa_{max} = 5$, and $a_{max} = 0.05$).
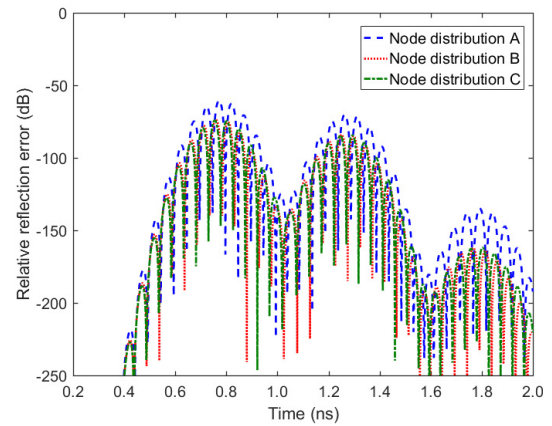

Fig. 7. Relative reflection errors versus time obtained with the proposed CFS-PML scheme with different node distribution types.
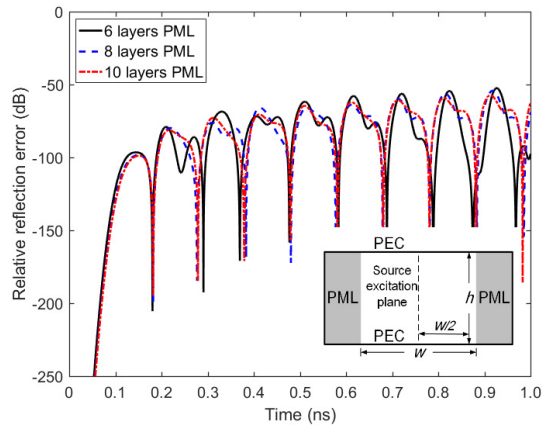

Fig. 8. Relative reflection errors of the parallel-plate waveguide operating under the cutoff frequency with the evanescent wave.

can inherently be deployed without much difficulty or additional process. The proposed CFS-PMLs truncate the solution domain in the horizontal direction, while the dimensions of the solution domain in the vertical direction are made long enough so that the reflections by the vertical ends do not reach the measurement points before the computation is terminated. In such a way, the reflections by the horizontal CFS-PMLs can be measured properly without the interferences from boundaries in the vertical directions. Three different CFS-PML node distributions are considered:

A) four layers of uniform node distribution,

B) the PML node density in the subspace close to the solution domain being 1.5 times higher than that in the other PML region, and

C) the PML node density in the subspace close to the solution domain being two times higher than that in the other PML region. The results are shown in Fig. 7. As can be seen, the obtained relative reflection errors are less than −60.4 dB in situation A with uniform node distributions.

The reflection error is reduced to be less than −73.6 and −74.1 dB in situations B) and C), respectively. This is because more nodes are used in the PML regions in situations B) and C), equivalent to more PML layers.

Finally, to study the PML absorption of evanescent waves, we consider a parallel-plate waveguide filled with air. The distance between the two PEC plates is $h = 30$ mm. The waveguide has a cutoff frequency at 5 GHz for TM_1 mode. A TM_1 of frequency $f_m = 2$ GHz (below the cutoff frequency) is excited, and the proposed PMLs are placed very close to the source plane, at only $w/2 = 3$ mm away from the source plane. This short distance of 3 mm guarantees that the evanescent mode still has a significant amplitude when it reaches the PMLs. The results are shown in Fig. 8. As can be seen, the reflection error is −52.5, −54.2, and −57.3 dB or less with six, eight, and ten PML layers. The results verify that the proposed CFS-PML scheme can also absorb the evanescent wave very well.

IV. CONCLUSION

In this communication, we develop the recursive convolutional CFS-PML ABC for the wave-equation-based meshless method. The effects of the CFS-PML parameters on the absorption performances are investigated. The impacts of the shape parameter of the meshless method and node distribution types are also analyzed. Numerical results confirm the generally good performances of the proposed formulations for the time-domain meshless method based on the wave equation. The relative reflection error of the proposed PML is less than −54.2 dB with eight PML layers even for evanescent waves. Future work may lie in application to heterogeneous medium [28] and multiphysics problems [29], which is underway in our research group, and the results are to be reported in the future.

REFERENCES

[1] A. Taflove, *Computational Electrodynamics: The Finite-Difference Time-Domain Method*. Boston, MA, USA: Artech House, 2005.

[2] J.-M. Jin, *The Finite Element Method in Electromagnetics*. New York, NY, USA: Wiley, 2002.

[3] R. F. Harrington, *Field Computation by Moment Methods*. Oxford, U.K.: Oxford Univ. Press, 1996.

[4] V. Cingoski, N. Miyamoto, and H. Yamashita, "Element-free Galerkin method for electromagnetic field computations," *IEEE Trans. Magn.*, vol. 34, no. 5, pp. 3236–3239, Sep. 1998.

[5] S. A. Viana and R. C. Mesquita, "Moving least square reproducing kernel method for electromagnetic field computation," *IEEE Trans. Magn.*, vol. 35, no. 3, pp. 1372–1375, May 1999.

[6] G. Ala, E. Francomano, A. Tortorici, E. Toscano, and F. Viola, "Smoothed particle electromagnetics: A mesh-free solver for transients," *J. Comput. Appl. Math.*, vol. 191, no. 2, pp. 194–205, Jul. 2006.

[7] J. G. Wang and G. R. Liu, "A point interpolation meshless method based on radial basis functions," *Int. J. Numer. Methods Eng.*, vol. 54, pp. 1626–1648, 2002.

[8] Y. Yu and Z. Chen, "A three-dimensional radial point interpolation method for meshless time-domain modeling," *IEEE Trans. Microw. Theory Techn.*, vol. 57, no. 8, pp. 2015–2020, Aug. 2009.

[9] Y. Yu and Z. Chen, "Implementation of material interface conditions in the radial point interpolation meshless method," *IEEE Trans. Antennas Propag.*, vol. 59, no. 8, pp. 2916–2923, Aug. 2011.

[10] S. Yang, Z. Chen, Y. Yu, and S. Ponomarenko, "On the numerical dispersion of the radial point interpolation meshless method," *IEEE Microw. Wireless Compon. Lett.*, vol. 24, no. 10, pp. 653–655, Oct. 2014.

[11] S. Yang, Z. Chen, Y. Yu, and S. Ponomarenko, "A divergence free meshless method based on the vector basis function for transient electromagnetic analysis," *IEEE Trans. Microw. Theory Techn.*, vol. 62, no. 7, pp. 1409–1415, Jul. 2014.

[12] S. Shams, A. Ghafoorzadeh-Yazdi, and M. Movahhedi, "A 3-D dispersive time-domain meshless formulation for frequency-dependent materials," *IEEE Trans. Antennas Propag.*, vol. 66, no. 2, pp. 1040–1045, Feb. 2018.

[13] Y. Yu and Z. Chen, "The CPML absorbing boundary conditions for the unconditionally stable meshless modeling," *IEEE Antennas Wireless Propag. Lett.*, vol. 11, pp. 468–472, 2012.

[14] S. Yang, Y. Yu, Z. Chen, and S. Ponomarenko, "A time-domain collocation meshless method with local radial basis function for electromagnetic analysis," *IEEE Trans. Antennas Propag.*, vol. 62, no. 10, pp. 5334–5338, Oct. 2014.

[15] R. Khalef, M. T. Benhabiles, F. Grine, and M. L. Riabi, "An unconditionally stable radial point interpolation meshless method based on the Crank–Nicolson scheme solution of wave equation," *IEEE Trans. Microw. Theory Techn.*, vol. 66, no. 8, pp. 3705–3713, Aug. 2018.

[16] V. Lombardi, M. Bozzi, and L. Perregrini, "A novel variational meshless method with radial basis functions for waveguide eigenvalue problems," *IEEE Trans. Microw. Theory Techn.*, vol. 66, no. 8, pp. 3714–3723, Aug. 2018.

[17] V. Lombardi, M. Bozzi, and L. Perregrini, "Evaluation of the dispersion diagram of inhomogeneous waveguides by the variational meshless method," *IEEE Trans. Microw. Theory Techn.*, vol. 67, no. 6, pp. 2105–2113, Jun. 2019.

[18] W. C. Chew and W. H. Weedon, "A 3D perfectly matched medium from modified Maxwell's equations with stretched coordinates," *Microw. Opt. Technol. Lett.*, vol. 7, no. 13, pp. 599–604, Sep. 1994.

[19] Y. Rickard, N. Georgieva, and W.-P. Huang, "A perfectly matched layer for the 3-D wave equation in the time domain," *IEEE Microw. Wireless Compon. Lett.*, vol. 12, no. 5, pp. 181–183, May 2002.

[20] J.-P. Berenger, "A perfectly matched layer for the absorption of electromagnetic waves," *J. Comput. Phys.*, vol. 114, no. 2, pp. 185–200, Oct. 1994.

[21] J. A. Roden and S. D. Gedney, "Convolutional PML (CPML): An efficient FDTD implementation of the CFS-PML for arbitrary media," *Microw. Opt. Technol. Lett.*, vol. 27, no. 5, pp. 334–338, Dec. 2000.

[22] J. Wang *et al.*, "The split-field PML absorbing boundary condition for the unconditionally stable node-based LOD-RPIM method," *IEEE Antennas Wireless Propag. Lett.*, vol. 17, no. 10, pp. 1920–1924, Oct. 2018.

[23] D. R. Burke and T. J. Smy, "A meshless based solution to vectorial mode fields in optical micro-structured waveguides using leaky boundary conditions," *J. Lightw. Technol.*, vol. 31, no. 8, pp. 1191–1197, Apr. 2013.

[24] H. Zhu, C. Gao, H. Chen, and Q. Yin, "Implementation of perfectly matched layer absorbing boundary condition for CN-RPIM method," *Electron. Lett.*, vol. 53, no. 6, pp. 417–419, Mar. 2017.

[25] W. Bao and F. L. Teixeira, "Performance analysis of perfectly matched layers applied to spherical FDTD grids," *IEEE Trans. Antennas Propag.*, vol. 66, no. 2, pp. 1035–1039, Feb. 2018.

[26] N. Feng, Y. Zhang, Q. Sun, J. Zhu, W. T. Joines, and Q. H. Liu, "An accurate 3-D CFS-PML based Crank-Nicolson FDTD method and its applications in low-frequency subsurface sensing," *IEEE Trans. Antennas Propag.*, vol. 66, no. 6, pp. 2967–2975, Jun. 2018.

[27] A. Cangellaris, C.-C. Lin, and K. Mei, "Point-matched time domain finite element methods for electromagnetic radiation and scattering," *IEEE Trans. Antennas Propag.*, vol. 35, no. 10, pp. 1160–1173, Oct. 1987.

[28] K. Berthou-Pichavant, F. Liorzou, and P. Gelin, "Wave propagation in heterogeneous anisotropic magnetic materials," *IEEE Trans. Microw. Theory Techn.*, vol. 45, no. 5, pp. 687–690, May 1997.

[29] X. Zhang, Z. Chen, and Y. Yu, "An unconditional stable meshless ADI-RPIM for simulation of coupled transient electrothermal problems," *IEEE J. Multiscale Multiphys. Comput. Techn.*, vol. 1, no. 5, pp. 98–106, Nov. 2016.

[30] J. Wang, Z. Chen, J. Li, Y. Yu, and J. Liang, "Towards a unifying computational platform with the node-based meshless method," in *IEEE MTT-S Int. Microw. Symp. Dig.*, Jun. 2018, pp. 1017–1020.